

West Chester University

Digital Commons @ West Chester University

Chemistry Faculty Publications

Chemistry

10-2020

Low-Load Metal-Assisted Catalytic Etching Produces Scalable Porosity in Si Powders

Konstantin Tamarov

Riku Kiviluoto

Josph D. Swanson

Bret A. Unger

Alexis T. Ernst

See next page for additional authors

Follow this and additional works at: https://digitalcommons.wcupa.edu/chem_facpub



Part of the [Materials Chemistry Commons](#)

Authors

Konstantin Tamarov, Riku Kiviluoto, Josph D. Swanson, Bret A. Unger, Alexis T. Ernst, Mark Aindow, Joakim Riikonen, Vesa-Pekka Lehto, and Kurt W. Kolasinski

Low-Load Metal-Assisted Catalytic Etching Produces Scalable Porosity in Si Powders

Konstantin Tamarov, Riku Kiviluoto, Joseph D. Swanson, Bret A. Unger, Alexis T. Ernst, Mark Aindow, Joakim Riikonen, Vesa-Pekka Lehto, and Kurt W. Kolasinski*

Cite This: <https://dx.doi.org/10.1021/acsami.0c13980>

Read Online

ACCESS |

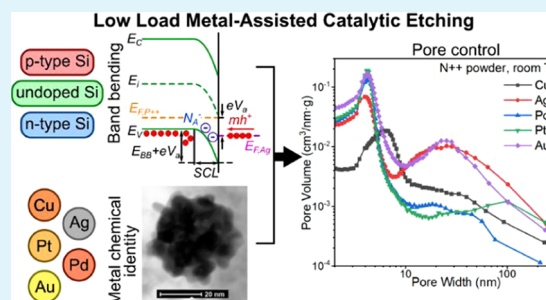
Metrics & More

Article Recommendations

Supporting Information

ABSTRACT: The recently discovered low-load metal-assisted catalytic etching (LL-MACE) creates nanostructured Si with controllable and variable characteristics that distinguish this technique from the conventional high-load variant. LL-MACE employs 150 times less metal catalyst and produces porous Si instead of Si nanowires. In this work, we demonstrate that some of the features of LL-MACE cannot be explained by the present understanding of MACE. With mechanistic insight derived from extensive experimentation, it is demonstrated that (1) the method allows the use of not only Ag, Pd, Pt, and Au as metal catalysts but also Cu and (2) judicious combinations of process parameters such as the type of metal, Si doping levels, and etching temperatures facilitate control over yield (0.065–88%), pore size (3–100 nm), specific surface area (20–310 m²·g⁻¹), and specific pore volume (0.05–1.05 cm³·g⁻¹). The porous structure of the product depends on the space-charge layer, which is controlled by the Si doping and the chemical identity of the deposited metal. The porous structure was also dependent on the dynamic structure of the deposited metal. A distinctive comet-like structure of metal nanoparticles was observed after etching with Cu, Ag, Pd, and, in some cases, Pt; this structure consisted of 10–50 nm main particles surrounded by smaller (<5 nm) nanoparticles. With good scalability and precise control of structural properties, LL-MACE facilitates Si applications in photovoltaics, energy storage, biomedicine, and water purification.

KEYWORDS: low-load metal-assisted catalytic etching (MACE), porous silicon, powder, porosity, nanoparticles, silicon nanostructures



INTRODUCTION

Metal-assisted catalytic etching (also known as metal-assisted etching or metal-assisted chemical etching), MACE, is a simple and versatile method of Si micropatterning. Nanostructuring of Si with MACE has attracted considerable attention in the past few years to fabricate nonreflecting surfaces for photovoltaics,^{1–3} to prepare patterned structures for sensing,^{4–6} and to overcome the huge volume expansion of Si-based Li-ion battery anodes.^{7–9} Porous Si nanowires (NWs) and nanoneedles formed by MACE have been used in a large number of different biological applications including sensing,¹⁰ studies of cell–Si interfaces,^{11,12} and therapeutic delivery.^{13–15}

Typically, MACE is performed in a two-step process (metal deposition and etching are performed separately)¹⁶ although one-step MACE (combined metal deposition and etching)^{17,18} has also been demonstrated successfully. In the two-step process, a piece of Si is first immersed into a metal plating solution consisting of hydrofluoric acid (HF), water, and dissolved metal salt, e.g., AgNO₃. Ag⁺ ions deposit as particles, dendrites, or layers on the Si surface, and this process can be further controlled by applying masks or even more sophisticated methods such as lithography, thermal decomposition, or sputtering. In the second step, the Si is immersed in a solution containing HF and oxidant, usually H₂O₂. The metal catalyst

facilitates hole injection into the Si valence band, which controls the rate of the etching reaction as long as the concentration of HF is sufficiently high.

Due to the high concentrations of holes near the metal/Si interface and generally high metal coverage, the most common outcome of MACE is the formation of 80–150 nm etch track pores bored by the cooperative motion of metal particles, which are formed dynamically at the beginning of etching.^{19,20} The walls of the pores are often called Si NWs, even though etching first forms interconnected walls and ridge-like structures that are cleaved readily by, e.g., ultrasound or capillary forces to form stand-alone Si NWs.

In an attempt to improve the cost-efficiency of the MACE process, several recent studies focused on etching inexpensive Si grains, chunks, and powders instead of wafers. It is especially interesting that even in powders, metal particles still move cooperatively, descend into Si perpendicular to particular

Received: August 3, 2020

Accepted: October 2, 2020

64 facets,¹⁹ and produce etch track pores and Si NWs similar to
65 MACE of wafers.

66 Thus, MACE was applied to inexpensive and relatively impure
67 metallurgical-grade (MG) powders. Preferential etching of the
68 impurities led to purification of Si,^{21,22} which made it possible to
69 apply the etched particles for Li-ion battery anodes^{23,24} and
70 photovoltaics²⁵ and to produce biocompatible nanostructures
71 for nanomedicine.²⁶

72 Scaling up MACE of powders requires control of the etching
73 process. The rate of this highly exothermic reaction is
74 proportional to the surface area. The high surface area of
75 powders compared to that of Si wafers leads to considerable heat
76 production during MACE. Thermal management during the
77 reaction is crucial to improve the uniformity and reproducibility
78 of the product. Similar to regenerative electroless etching
79 (ReEtching),²⁷ we exploited a syringe pump to inject oxidant at
80 a constant rate, giving better control over MACE and avoiding
81 excessive heating. In addition, we demonstrated the use of a
82 syringe pump to deposit Ag controllably. Combined with
83 vigorous stirring of Si powder and addition of acetic acid to HF,
84 we achieved uniform Ag deposition over a wide range of $n(\text{Ag}) \cdot$
85 A_{Si}^{-1} , from 10 to 0.002 mmol·m⁻², where $n(\text{Ag})$ is the amount of
86 silver and A_{Si} is the surface area of the Si powder subjected to
87 MACE.²⁰

88 Varying the Ag coverage, we demonstrated that large etch
89 track pores produced by the correlated motion of metal catalyst
90 nanoparticles and Si NWs are not the only outcome of Ag
91 MACE.²⁰ When the Ag amount is low in the depositing solution
92 ($n(\text{Ag}) \cdot A_{\text{Si}}^{-1} \leq 0.06$ mmol·m⁻²), Ag deposits as individual 10–
93 20 nm nanoparticles instead of a thick layer of interconnected
94 clusters and dendrites. During etching, these small nanoparticles
95 move in an uncorrelated manner producing random pores with
96 10–20 nm diameter and, if the p-type doping level is high
97 enough, 4–6 nm tortuous pores. Thus, a mesoporous layer is
98 formed in contrast to Si NWs. We call this regime low-load
99 MACE or LL-MACE to emphasize its difference from
100 conventional high-load MACE or HL-MACE.

101 For a comprehensive discussion of HL-MACE, and structures
102 accessible through this process, we refer to the recent review by
103 Alhmod et al.²⁸ Here, we summarize a few salient points.
104 Depending on the metal catalyst, Si doping level, and oxidant
105 amount, the porosity of etch track pore walls and Si NWs in HL-
106 MACE can be varied. Etching highly doped p-type Si ($\rho = 0.01$ –
107 0.02 Ω ·cm) with Ag generally resulted in NWs with porous
108 walls, while lower doping levels led to solid Si NWs.^{29,30} Etching
109 with Au produced porous Si NWs for a Si resistivity of up to 1 Ω ·
110 cm, depending on the H₂O₂ concentration.³¹ Pt formed both a
111 porous layer and helical etch track pores on 10 Ω ·cm p-type
112 wafers; the latter was attributed to the multifaceted crystalline
113 shape of the Pt particles. Pd was found to be more convoluted
114 than others as it catalyzed etching even without an oxidant and
115 resulted in electropolishing of Si.^{32–34} HL-MACE with Cu never
116 produced defined etch track pores^{35,36} and Si NWs, except in the
117 case of electrochemical etching under applied bias.³⁷ This is due
118 to the low electronegativity and reduction potential of Cu
119 compared to those of other metals, which prevents efficient
120 deposition and leads to enhanced dissolution during etching.
121 Overall, depending on the chemical identity of the metals, their
122 catalytic activity toward the reduction of H₂O₂, and induced
123 band bending,^{33,38,39} different morphologies were produced by
124 HL-MACE.

125 Herein, we present a comprehensive study of LL-MACE of Si
126 powders, where we use low amounts of Cu, Ag, Au, Pt (12 μ mol·

m⁻²), and Pd (1.2 μ mol·m⁻²) to etch mesopores. Various Si
127 grades were used including powders prepared from P++, P+, P,
128 N+, N++, and undoped wafers (UW) as well as metallurgical-
129 grade powders with either 99.6% (MG) or 99.997% (MC10)
130 purity. We demonstrate that by choosing Si grade, metal, and
131 temperature, one can vary over a wide range the yield (0.065–
132 88%), pore size (3–100 nm), surface area (20–310 m²·g⁻¹), and
133 pore volume (0.05–1.05 cm³·g⁻¹).
134

135 Overall, we found a great variety of porosity after LL-MACE.
136 This can be applied to optimize porosity and surface area for
137 applications such as Si-based Li-ion battery anodes, antire-
138 flection coatings for photovoltaics, and to load drugs or
139 biomolecules of a specific size. Furthermore, LL-MACE is
140 easy to scale up, uses minimal amounts of metal, and works well
141 for certain Si grades with Cu, opening a pathway to significantly
142 less expensive processing.

143 ■ EXPERIMENTAL SECTION

144 Samples were prepared and characterized in line with previously
145 published methods.^{20,32,40} Briefly, Si powders of known purity/doping
146 levels were milled and cleaned prior to the deposition and nucleation of
147 a metal catalyst. Subsequently, etching was initiated by the addition of
148 oxidant (H₂O₂). Both nucleation and etching were aided by the use of
149 acetic acid as a surfactant and steady metered injection of dissolved
150 metal ions or H₂O₂ with a syringe pump. The sample temperature
151 during reaction was regulated by immersing the reaction vessel in either
152 an ice/water or temperature-controlled water bath. After well-defined
153 rinsing and drying procedures, the samples were characterized by plain-
154 view and cross-sectional scanning electron microscopy (SEM) with
155 focused ion beam (FIB) cutting. FIB sectioning was also used to
156 prepare samples for transmission electron microscopy (TEM). Further
157 characterization was performed with N₂ sorption followed by analysis
158 with the Brunauer–Emmett–Teller (BET) model and Barrett–
159 Joyner–Halenda (BJH) theory. The detailed methods can be found
160 in the [Supporting Information](#).

161 ■ RESULTS

162 Controlled injection together with acetic acid as a surfactant
163 resulted in the uniform coverage of Si surfaces with individual
164 5–30 nm metal nanoparticles separated by similarly sized
165 gaps.^{20,32} Specifically for Ag,²⁰ we found deposited nanoparticles
166 with a mean size of 19.0 \pm 9.5 nm and a center-to-center
167 separation of 25.6 \pm 9.0 nm (uncertainty given as 1 standard
168 deviation) to be responsible for catalyzing efficient etching in the
169 LL-MACE regime. These values were calculated under the
170 assumption that the particle surfaces were perfectly planar. As
171 shown previously,²⁰ these well-spaced nanoparticles move in a
172 completely uncorrelated manner during etching, following paths
173 determined by the minimum energy required to etch out one
174 atomic plane of Si.

175 In the etching step of LL-MACE, the H₂O₂ solution was also
176 injected in a controlled manner using a syringe pump; this
177 provided a minimal steady-state supply of the oxidant that
178 significantly reduced the rate of heat generation. In most cases,
179 the temperature of the etching solution did not exceed the
180 temperature of cooling the bath by more than 12 °C. It should be
181 stressed that, while Ag, Pd, Pt, and Au are commonly applied in
182 HL-MACE,¹⁶ Cu is never used because it fails to deposit on Si in
183 a sufficient quantity and it dissolves efficiently in the presence of
184 excess H₂O₂. However, the use of a syringe pump for the dosing
185 of H₂O₂ enables us to reduce its steady-state concentration to a
186 level that does not remove Cu nanoparticles from the etch front.

187 Application of different metals in LL-MACE resulted in
188 distinctive morphologies of etched pores, yet they also had some

189 common features. Top-view SEM images (Figure 1 and Sections
190 S3–S6, Supporting Information) show that Cu and Pt keep the

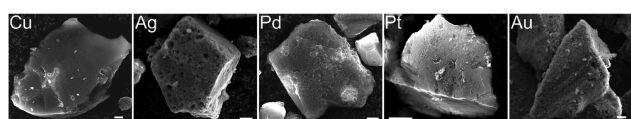


Figure 1. General view of 11–25 μm MG Si particles after LL-MACE with Cu, Ag, Pd, Pt, and Au. The scale bar represents 2 μm .

191 Si particle surfaces flat and edges sharp. A unique feature of Pt
192 particles is that they tend to move laterally across the Si surface
193 producing many, sometimes helical channels before descending
194 into Si. Ag, Pd, and Au, on the other hand, smoothen Si edges
195 while roughening initially flat facets, which produces a fuzzy
196 appearance that is distinctly different from the texture of
197 particles produced by HL-MACE.

198 Cross-sectional images are presented in Figure 2. An enlarged
199 version of Figure 2 with additional annotation can be found in
200 the Supporting Information (Figure S2.1). These images reveal
201 that the etched Si for all metals consisted of two distinct regions:
202 (1) etch track pores in the direction of the metal nanoparticle
203 movement and (2) a layer of tortuous pores surrounding the
204 tracks or extending deep into Si. The tortuous pores were similar
205 to those observed in ReEtching of Si powders, where no metal
206 catalyst was deposited on P++ and MG Si.²⁷ For Cu, Ag, and Pd,
207 tortuous pore regions tended to surround etch track pores
208 making the boundary between etched and bulk Si uneven,
209 composed of connected spherical regions. Cu nanoparticles
210 sometimes were not surrounded by tortuous pores. In contrast,
211 the boundary between tortuous pores and bulk Si for Pt and Au
212 was remarkably flat despite different Pt and Au particle
213 morphologies (Figure 2). The observation of both etch track
214 and tortuous pores is consistent with previous results such as
215 those of Hochbaum et al.,⁴¹ who were the first to observe porous
216 nanowire formation, Chiappini et al.,³¹ and Patil et al.⁴²

217 The dynamic nature of the metal nanoparticle structure
218 caused by the etch process is illustrated by a comet-like structure
219 reported here for the first time (Figures 2 and S2.1 and Sections
220 S3–S6, Supporting Information). Cu and Pd nanoparticles had
221 rather smooth although not round surfaces, and they were
222 always followed by a halo of small <5 nm nanoparticles. The
223 large metal nanoparticles form the cores of these comet-like
224 structures; they were 50–80 nm for Cu and 30–50 nm for Pd.
225 Interestingly, Cu “comets” have small nanoparticle “tails” behind
226 their etch track, while Pd “comet” cores were surrounded by
227 small nanoparticles on all sides. Pt particles possessed rich
228 irregular structures, which appear to form by aggregation at the
229 beginning of etching when particles moved extensively along the
230 Si surfaces. These aggregates expose different Pt crystalline
231 planes, which, we suggest, make the change of etch direction
232 easy and, in some cases, produce helical cavities. Despite the
233 previously considered stability of Pt particles during MACE,
234 they sometimes, although not always, showed comet-like
235 structures and were surrounded by small nanoparticle satellites.
236 Au nanoparticles were the most stable and round; they never
237 showed a halo of small nanoparticles and kept their sizes in the
238 range of 10–40 nm during etching.

239 The outcomes of LL-MACE changed dramatically with the
240 metal catalyst, Si grade (Table 1), and temperature (Figure 3
241 and Sections S3–S12, Supporting Information). In SEM images,
242 Cu displays the most prominent change in structure with the

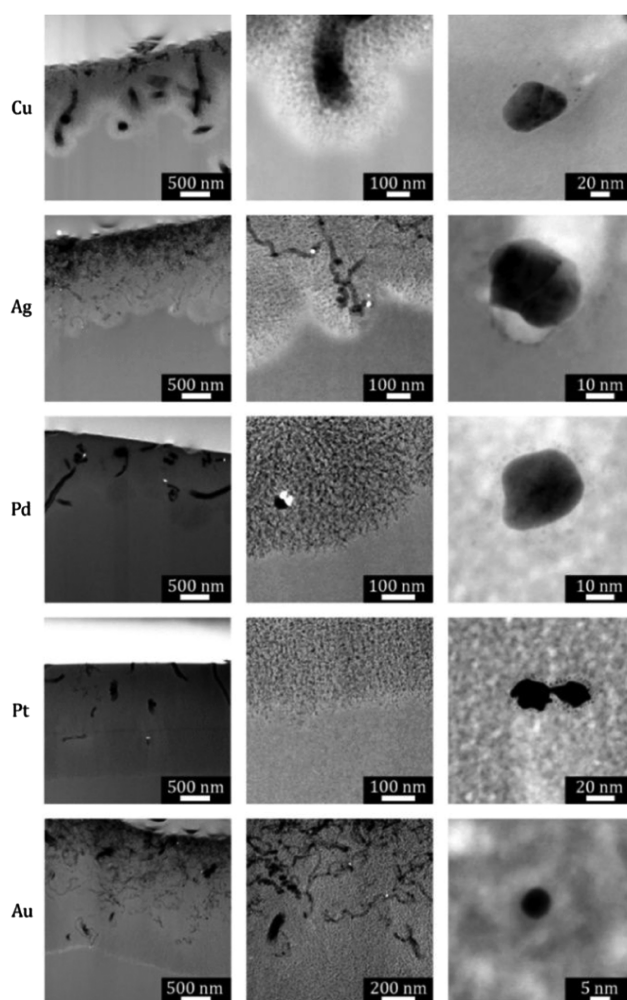


Figure 2. Cross-sectional bright-field (BF) and high-angle annular dark-field (HAADF) scanning transmission electron microscopy (STEM) images after LL-MACE of 11–25 μm P++ (for Cu) and 2–44 μm MG (for other metals) powders in an ice bath. The left column (HAADF, metal appears light) shows the border between the bulk and etched Si: Cu and Pd produce an irregular border and tortuous pores surrounding metal particles; Pt and Au present a sharp and uniform border between the porous layer and solid core. The middle column (HAADF) takes a closer look at the porous layer showing both etch track pores produced by the metal particle movement and tortuous mesopores produced by remote etching. The right column (BF, metal appears dark) depicts the structure of metal particles: Cu and Pd always present a halo of small particles following big ones; Pt sometimes presents a halo of small particles and the large particles have an irregular structure; Au never shows the halo. An enlarged, annotated version of this figure and more images of metal particles are shown in the Supporting Information.

243 increasing temperature. For low-temperature (LT) etching in an
244 ice bath, Cu particles descend into Si and produce pores. At high
245 temperature (HT, water bath at 43 $^{\circ}\text{C}$), most of the Si becomes
246 electropolished: P++, MG, and MC10 present broken Si pieces
247 with smooth surfaces, while UW and N++ have macropores with
248 crystallographically defined edges. N++ powder additionally
249 presents numerous uniformly distributed openings of tortuous
250 pores at HT (Figures 3 and S3.10, Supporting Information).
251 Other metals demonstrate less pronounced differences between
252 LT and HT. One can notice similarity for powders etched with
253 Ag and Au. Pd and Pt show distinctive morphologies, which, 254
255 however, look similar for all Si grades. Pt is the only case that

Table 1. Summary of the Si Particle Sizes and Grades Used in LL-MACE^a

abbreviation	resistivity ($\Omega\cdot\text{cm}$)	doping type	doping density (cm^{-3})	particle size (μm)
P++ ^b	0.0186	boron	4×10^{18}	11–25
P+ ^b	0.105	boron	3×10^{17}	11–25
P ^b	25	boron	5×10^{14}	11–25
UW ^b	>5000	boron	$<1 \times 10^{12}$	11–25
N+ ^b	1.15	phosphorus	3×10^{15}	11–25
N++ ^b	0.0144	phosphorus	3×10^{18}	11–25
MG ^{c,d}		Fe/Ti/Ca/Al		11–25
MC10 ^{c,e}		Fe/Ti/Ca/Al		1.5–10

^aDopant concentrations were calculated using the Caughey–Thomas expression⁴³ for electron and hole mobilities. ^bGround single-crystal (100) wafers from Okmetic Oy, Finland. ^cMetallurgical-grade Si from Elkem Silicon Materials, Norway. ^dPurity: 99.8%. ^ePurity: 99.997%.

allows easy observation of the openings of tortuous pores on SEM images and the increase of their diameters with the increase of temperature.

Measured pore size distributions for P++, UW, and N++ powders (Figure 4) and for MG and MC10 powders (Figure S13.1, Supporting Information) after LL-MACE at three temperatures reveal quantitative insights into the structure of etched Si because the presence or absence of tortuous pores (<10 nm) can be easily recognized. It should be noted here that the Barrett–Joyner–Halenda (BJH) analysis applied to N₂ desorption isotherms is not sensitive for large pores (>75 nm). Therefore, etch track pores, for example, produced by Pt particles, are not visible in the pore size distributions.

Cu is the metal with the lowest reduction potential, and it readily dissolves especially at HT, when holes are injected into it at a higher rate than at LT and room temperature (RT). Consequently, it may be anticipated that Cu LL-MACE either (1) partially follows a ReEtching-like mechanism where Cu ions inject holes into Si directly and then get regenerated by H₂O₂ to repeat the process and/or (2) preferentially adsorb at step and defect sites on the Si surfaces akin to underpotential deposition, which in turn causes step-flow etching rather than porosification.

The latter observation is consistent with the observation of crystallographically defined etched features noted above. The combination of these effects results in complete electropolishing of Si at HT. At LT, Cu is capable of producing tortuous pores for highly doped P++ and N++ powders (Figure 4) and MG (Section S3, Supporting Information). The increase of the etching temperature to RT and HT for P++ Si results in the formation of mostly etch track pores by comet-like particles. In the case of N++ powder, tortuous pores were observed at all temperatures. Their volume was the highest in N++ among all Si grades and their average width increased with the temperature. We attribute this to the partial recombination of injected holes, which prevented electropolishing. For UW wafer, a minor component of etching is the formation of pores below 100 nm, while macropore formation represents the majority (Figure 3).

Use of Ag significantly changes the outcome of LL-MACE compared to that of Cu-catalyzed etching (Figure 4 and Section S4, Supporting Information). The volume of tortuous pores for P++ powder at LT ($0.037 \text{ cm}^3 \cdot \text{g}^{-1}$) is much smaller than for Cu ($0.18 \text{ cm}^3 \cdot \text{g}^{-1}$; Tables S3.2 and S4.2, Supporting Information) and increases with increasing temperature (note the different y-axis scales in the graphs). Etch track pores produced by 10–30 nm Ag particles are clearly visible. They become wider at HT, possibly due to high hole injection and Si polarization, which results in an additional etching around Ag particles and thus pore widening. In UW powder, Ag is only able to make etch track pores, while in N++ tortuous pores were observed again and in higher volume than in P++.

Pd is the most peculiar among the metals. Pd loading had to be decreased by a factor of 10 to avoid complete Si dissolution. Pd was found to create a moderate number of tortuous pores in P++ and a high number in N++ powder, while UW powder is mostly electropolished (Figure 4). The average pore width increased for the former cases with the increase of temperature along with the decrease of volume. We attribute this to the enhanced electropolishing triggered by a higher rate of hole injection into Si at RT and HT. N++ Si at HT was completely dissolved (yield was 0.06%). Etch track pores were hardly

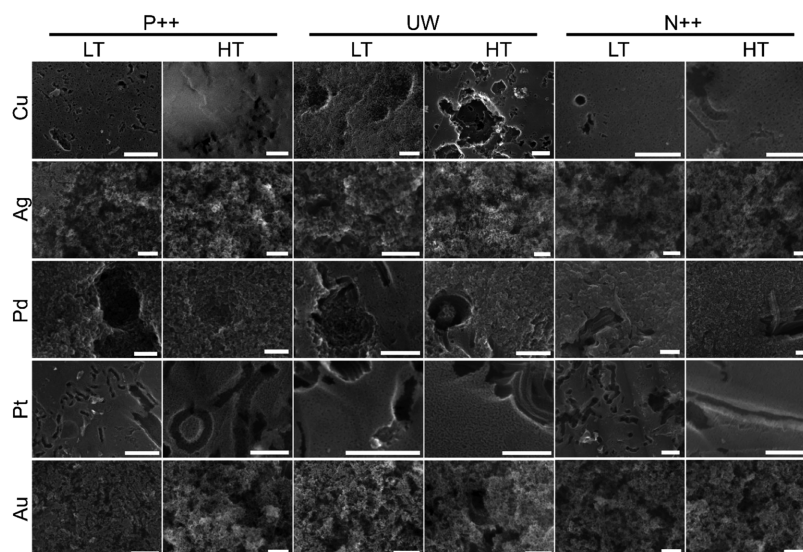


Figure 3. SEM images of the outer surfaces of Si particles after LL-MACE of P++, UW, and N++ 11–25 μm powders with different metals. Low-temperature (LT) and high-temperature (HT) columns show particles etched in an ice bath and water bath at 43 °C, respectively. The scale bar represents 200 nm.

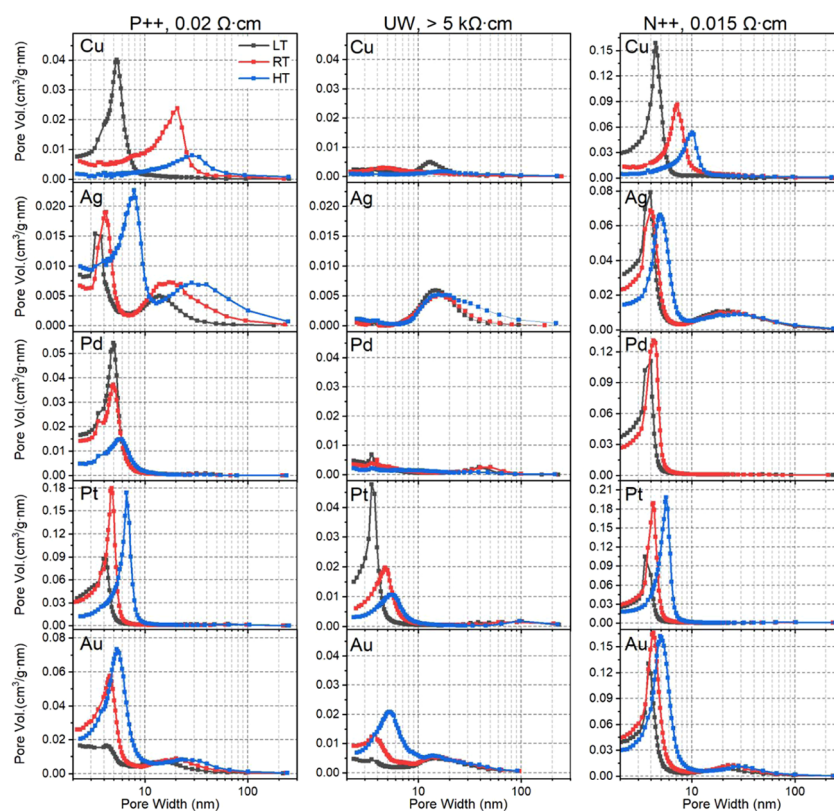


Figure 4. BJH pore size distributions of P++, UW, and N++ powders after Cu, Ag, Pd, Pt, and Au LL-MACE at three different temperatures: low temperature (LT, ice bath), room temperature (RT, water bath), and high temperature (HT, water bath at 43 °C).

315 observed (small peak around 40–50 nm) in the few Si particles
316 that remain.

317 Pt and Au are the two metals that could etch tortuous pores in
318 all Si grades (Figure 4). Notably, Pt did not distinguish between
319 P++ and N++ powders. Pore sizes and volumes are very similar
320 in both cases; the average pore widths and volumes increased
321 with the increase of etching temperature. In Au LL-MACE,
322 tortuous pore volumes for N++ powder were 1.6 ± 0.1 times
323 higher than for P++. Pore volumes, just as for Pt, grew with the
324 increase in temperature. However, for UW powder, the pore size
325 and volume change as a function of temperature are opposite for
326 Pt and Au. While for Pt the volume of tortuous pores decreases
327 from 0.17 to 0.04 $\text{cm}^3 \cdot \text{g}^{-1}$, for Au it grows from 0.02 to 0.11 $\text{cm}^3 \cdot$
328 g^{-1} with the change from LT to HT. Note here again the clear
329 presence of etch track pores produced by 10–40 nm Au
330 nanoparticles similar to that of the Ag ones. This explains the
331 resemblance between SEM images in Figure 2 for Ag and Au.
332 However, that is the only resemblance between them; Au clearly
333 outperforms Ag in the etching of tortuous <10 nm pores for all Si
334 grades.

335 The specific characteristics of P++, UW, and N++ powders
336 after LL-MACE are summarized in Figure 5, and for MG and
337 MC10 powders in Figure S13.2 (Supporting Information). It
338 can be seen that applying different metals, Si grades, and
339 temperatures, a wide range of specific surface areas, pore
340 volumes, and yields are accessible through LL-MACE. Depend-
341 ing on the etching parameters, surface areas were found to vary
342 from 14 to 310 $\text{m}^2 \cdot \text{g}^{-1}$, pore volumes from 0.07 to 1.03 $\text{cm}^3 \cdot \text{g}^{-1}$,
343 and yields from 0.06 to 80%. The lowest values for surface areas
344 and pore volumes were measured for Cu and Pd, especially for
345 UW powder at HT. The highest values were unexpectedly
346 measured for N++ powder etched with Au. Yields were the

lowest when electropolishing appeared, particularly for Cu and
347 Pd at HT. 348

A general correlation between specific surface area and pore
349 volume can be observed; their increase (or decrease) correlates
350 with each other in most etchings. Yield, however, does not show
351 such a good correlation in many cases. This discrepancy is
352 because pore volumes were quantified with N_2 sorption and
353 calculated using the BJH method, which is applicable to
354 mesopore and small macropore range (2–75 nm). On the other
355 hand, yield accounts for all Si removed by the etch track pore
356 formation, etching of tortuous pores, and electropolishing. To
357 quantify the relative contribution of mesopores to the total
358 amount of Si etched, we introduce the ratio of $v_{\text{pore}}/v_{\text{etched}}$. It
359 connects two measured values: pore volume δ_{pore} from BJH
360 analysis and yield. The ratio can be calculated using the
361 following equation (see the derivation in Section S1.4,
362 Supporting Information) 363

$$\frac{v_{\text{pore}}}{v_{\text{etched}}} = \frac{\delta_{\text{pore}} \rho_{\text{Si}} Y}{(1 - Y)} \times 100\% \quad (1) \quad 364$$

where δ_{pore} [$\text{cm}^3 \cdot \text{g}^{-1}$] is the specific BJH pore volume, i.e., the
365 volume of pores significantly smaller than ~ 100 nm, $\rho_{\text{Si}} = 2.33$ $\text{g} \cdot$
366 cm^{-3} is the bulk density of Si, and Y is the yield. 367

When $v_{\text{pore}}/v_{\text{etched}}$ is close to 0%, but the yield is high, most of
368 the etching produced macropores. If $v_{\text{pore}}/v_{\text{etched}}$ is close to 0%
369 and the yield is also small (Cu and Pd at HT), electropolishing
370 took place. Ag produced only etch track pores in UW powder
371 and $v_{\text{pore}}/v_{\text{etched}} = 10\%$. High values of $v_{\text{pore}}/v_{\text{etched}}$ (as high as
372 50–90%), specific surface area, and pore volume were found for
373 Pt. Thus, Pt is the optimal catalyst to form mostly tortuous <10
374 nm pores; the large etch track pores visible on SEM images 375

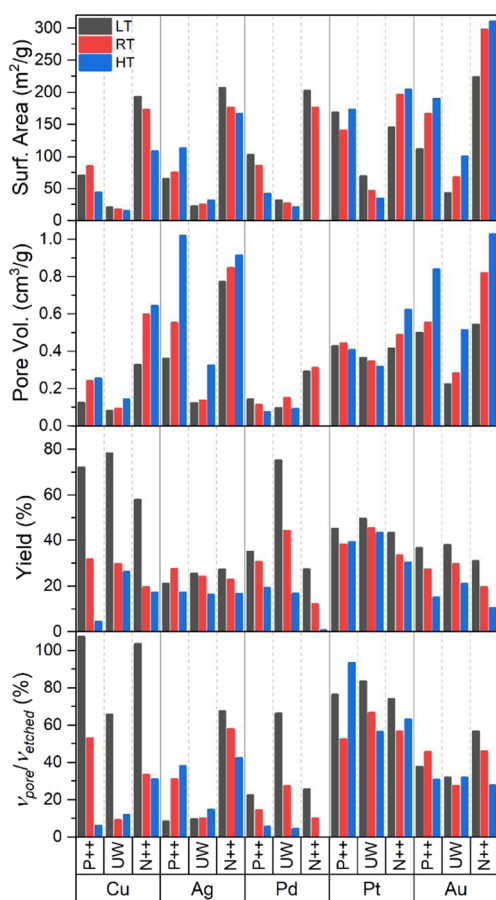


Figure 5. BET specific surface area, yield, BJH pore volume, and ratio of $v_{\text{pore}}/v_{\text{etched}}$ for P++, UW, and N++ powders after Cu, Ag, Pd, Pt, and Au LL-MACE at three different temperatures. The value of $v_{\text{pore}}/v_{\text{etched}}$ describes the ratio of the BJH pore volume (pores < 150 nm) to the total volume of etched-out Si.

Au is the optimal catalyst for etching of tortuous pores in all Si grades. It is the metal that created the highest specific surface areas of 310 m²·g⁻¹ for N++ powder and 190 m²·g⁻¹ for P++ powder, and it is the only catalyst to produce up to 100 m²·g⁻¹ surface area and 0.5 cm³·g⁻¹ pore volume in UW Si at HT. The ratio of $v_{\text{pore}}/v_{\text{etched}}$ adopts moderate values of 25–50% depending on temperature, possibly due to etch track pores that are larger than 100 nm and/or partial electropolishing.

Finally, we compared all of the Si grades at specific temperatures for all metals to (1) understand the role of impurities in MG and MC10 powders and (2) evaluate the effect of intermediate dopant levels in P+, P, and N+ powders on pore size distributions (Figure 6). The temperatures were selected to avoid electropolishing and to produce a high number of tortuous pores. Specific surface areas, pore volumes, yields, and $v_{\text{pore}}/v_{\text{etched}}$ values can be found in Section S14, Supporting Information. Figure 6 demonstrates unambiguously that there is a threshold for the appearance of a high volume of tortuous pores. They are etched efficiently in highly doped nearly metallic P++ and N++ powders, as well as 99.6% pure MG Si, independent of the metal catalyst used. Interestingly, N++ outperforms P++ in all cases, although it was generally considered that in MACE remote etching appears mainly in the highly doped p-type Si.²⁸ All moderately doped Si powders, UW Si, and 99.997% pure MC10 powder show nearly the same outcome. MC10 has somewhat larger pore volumes and surface areas than P+, P, UW, and N+ powders because of the smaller particle size, 1.5–10 μm compared to 11–25 μm for others. Thus, a higher initial exterior surface area is accessible for etching. The only difference between P+, P, UW, and N+ powders can be observed for Pt-etched P+ Si, which has a larger volume of tortuous pores than the others. MG powder is somewhere in between N++ and P++. With Cu, MG resembles N++, while with Au it resembles P++.

DISCUSSION

Mechanism of LL-MACE. The presence of a hole near the Si surface is the essential requirement to initiate Si etching in HF-based solutions. Holes polarize surface Si–H bonds making them susceptible to fluoride ion attack and eventually resulting

account for a minority of the etched Si. Pt is, however, limited to producing a relatively small surface area for UW powder.

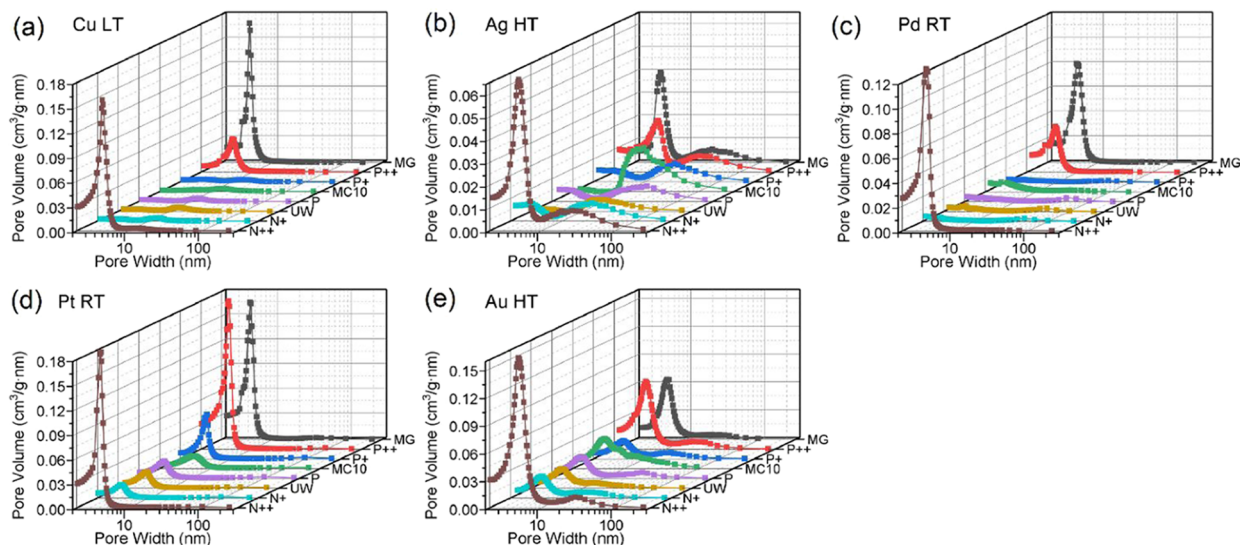


Figure 6. BJH pore size distribution after (a) Cu, (b) Ag, (c) Pd, (d) Pt, and (e) Au LL-MACE of different Si grades at the selected temperatures. The temperatures producing a high volume of tortuous pores are shown.

Table 2. Summary of Band Bending Magnitudes, Types, and Widths of Space-Charge Layers Formed Due to Metal Deposition on Si in an Ideal Case with Doping Types and Densities Used in LL-MACE

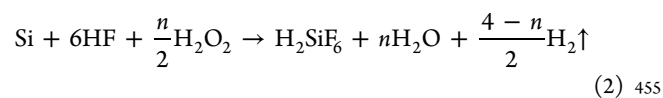
Si type E_F (eV) ^a	Cu 4.94 eV ^b	Ag 4.74 eV valence 2 ^c	Pd 5.6 eV valence 2/4	Pt 5.93 eV valence 4	Au 5.31 eV valence 2
P++	-0.37 eV ^d /8.6 nm ^e	-0.57 eV/10 nm	0.29 eV/1.4 nm	0.62 eV/1.4 nm	0.004 eV/1.4 nm
0.04	P depletion ^f	P depletion	P accumulation/degeneracy	P accumulation/degeneracy	P weak accumulation
P+	-0.3 eV/23 nm	-0.5 eV/28 nm	0.36 eV/5.3 nm	0.69 eV/5.3 nm	0.07 eV/5.3 nm
0.11	P depletion	P depletion	P accumulation/degeneracy	P accumulation/degeneracy	P weak accumulation
P	-0.14/169 nm	-0.34 eV/230 nm	0.52 eV/130 nm	0.85 eV/130 nm	0.23 eV/130 nm
0.27	P depletion	P depletion	P accumulation/degeneracy	P accumulation/degeneracy	P accumulation
UW	0.02/4 μm	-0.18 eV/1.5 μm	0.68 eV/2.9 μm	1.01 eV/2.9 μm	0.39 eV/2.9 μm
0.43	P weak accumulation	P depletion	P accumulation/degeneracy	P accumulation/degeneracy	P accumulation
N+	0.48/320 nm	0.28 eV/250 nm	1.14 eV/200 + 60 nm	1.47 eV/200 + 60 nm	0.85 eV/200 + 60 nm
0.88	N depletion	N depletion	N depletion + inversion	N depletion + inversion	N depletion + inversion
N++	0.66/21 + 6 nm	0.46/9.9 nm	1.32 eV/21 + 6 nm	1.65 eV/21 + 6 nm	1.03 eV/21 + 6 nm
1.06	N depletion + inversion	N depletion	N depletion + inversion	N depletion + inversion	N depletion + inversion

^aFermi energy E_F is calculated from the top of the valence band E_V , which is set to 0. Si work function in bulk is $\Phi_{\text{Si}} = \chi_{\text{Si}} + E_g - E_F$, where χ_{Si} is the Si electron affinity and E_g is the band gap. ^bMetal work functions Φ_M for (111) planes are taken from ref 56. ^cMolar stoichiometry $n(\text{VO}_2^+)/n(\text{Si})$ for MACE with VO_2^+ . ^dIdeal magnitudes of band bending E_{BB} calculated by subtracting the Si work function Φ_{Si} from metal work function Φ_M . For $E_{\text{BB}} < 0$, valence and conduction band edges bend downwards (hole depletion for the p-type Si), for $E_{\text{BB}} > 0$ —upwards (electron depletion for the n-type Si). ^eSchottky depletion space-charge layer D_{dep} width was calculated using eq S15.1 (Supporting Information). Equation S15.4 was used for inversion layer width. The width of the accumulation layer is the Debye length L_D calculated using eq S15.3. ^fClassification of the space-charge layer based on the doping type, density, and magnitude of band bending E_{BB} .

417 in the dissolution of Si. Various Si etching methods, including
418 electrochemical anodization, stain etching, and MACE, require
419 holes and they satisfy it using different approaches. In
420 electrochemical anodization of Si, holes present in Si due to
421 doping, light illumination, or spontaneous bulk generation are
422 directed to the surface by an applied bias. To form porous Si, the
423 bias should induce a small enough current density to make the
424 current-doubling pathway of Si dissolution dominant. In this
425 pathway, an injection of 1 hole into the valence band and 1
426 electron into the conduction band (that is, a valence 2 process)
427 is involved in the dissolution of 1 Si atom.⁴⁴ With the increase of
428 bias strength, the current-quadrupling (valence 4) pathway
429 involving 4 holes per Si atom becomes dominant and results in
430 complete dissolution of Si, i.e., above-critical-current density
431 etching. In stain etching, a strong oxidant (such as HNO_3)
432 present in the HF solution is able to oxidize Si directly, thus
433 injecting holes into the valence band.⁴⁵ Depending on the
434 concentrations, stain etching can form porous Si or extremely
435 flat surfaces by electropolishing.

436 In MACE, H_2O_2 is the most commonly used oxidant.^{16,28} It
437 has very poor hole injection kinetics into the Si valence band,
438 and the etch rate in $\text{HF}/\text{H}_2\text{O}_2$ is far below $0.005 \text{ nm}\cdot\text{s}^{-1}$ ⁴⁶ for the
439 H_2O_2 concentrations used in this study. The inability of H_2O_2 to
440 induce Si etching directly is possibly due to the need to break
441 H_2O_2 into two $-\text{OH}$ radicals for charge transfer to occur. In HF
442 solutions, Si surfaces are H-terminated and cannot dissociate
443 H_2O_2 at an appreciable rate. Thus, a catalyst is necessary to
444 reduce H_2O_2 and to inject holes into Si; many different metals
445 were studied for MACE including most commonly Ag, Au, Pd,
446 Pt,^{16,28,32} and Cu³⁶ and more exotically Ru,⁴⁷ Rh,⁴⁸ and Ni.⁴⁹ Ag
447 and Au are the most frequently applied catalysts, as their high
448 loading forms ordered arrays of Si NWs after HL-MACE. Cu
449 does not deposit well on Si surfaces and dissolves after oxidation
450 with high-concentration H_2O_2 , thus making it impossible to etch
451 Si NWs.

452 The electrochemical reactions involved in MACE consist of a
453 cathodic reaction on the metal catalyst and an anodic reaction
454 on Si. The overall reaction can be written as^{16,50}



455 where n can be 2, 3, or 4. $n = 2$ is the valence 2 or current-
456 doubling pathway, which is attributed to the formation of porous
457 Si and porous Si NWs during MACE (or more precisely HL-
458 MACE).⁵¹ When $n = 4$, the current-quadrupling or valence 4
459 pathway is in action, which can trigger electropolishing⁵² or
460 porosification, based on the model first proposed by Kooij and
461 Vanmaekelbergh⁵³ and explained in detail by Kolasinski et al.³² n
462 = 3 results from a mixture of divalent and tetravalent processes.
463 In HL-MACE, it is believed that etching above the critical
464 current density for porosification occurs in the vicinity of metal
465 particles because the concentration of holes injected into Si is
466 the highest there. However, some of the holes can diffuse further
467 from the metal particles. These holes induce nonlocal or remote
468 etching typically in the current-doubling regime producing
469 porous Si and porous Si NWs.
470

To determine the prevailing pathway, Chartier et al.⁵¹
471 suggested using the ratio of HF and H_2O_2 concentrations
472

$$\rho = \frac{[\text{HF}]}{[\text{HF}] + [\text{H}_2\text{O}_2]} \quad (3)$$

473 They found that for Ag HL-MACE and $\rho \geq 0.8$ the reaction
474 proceeded predominantly according to the valence 2 pathway,
475 while for $\rho \leq 0.2$ a valence 4 pathway and electropolishing were
476 observed with no Si NWs formed. In the middle range of $0.2 \leq \rho$
477 ≤ 0.8 , the mixture of pathways was present. This is currently the
478 widely accepted view on the HL-MACE mechanism supported
479 by many studies^{28,33} and comprehensively investigated for p-
480 type Si wafers.³¹
481

482 Applying this criterion to LL-MACE, ρ would be equal to 0.92
483 if all 0.037 mol of H_2O_2 were added initially to the etching
484 solution. However, ρ is never this large because during injection
485 H_2O_2 reacts at a rate that is comparable to the rate of injection.
486 This maintains a very low steady-state value of $[\text{H}_2\text{O}_2]$
487 throughout etching. Thus, if we were to extrapolate the ρ
488 dependence of etching in the presence of Ag to other metals, the
489 current-doubling pathway should be the dominant one for LL-
490

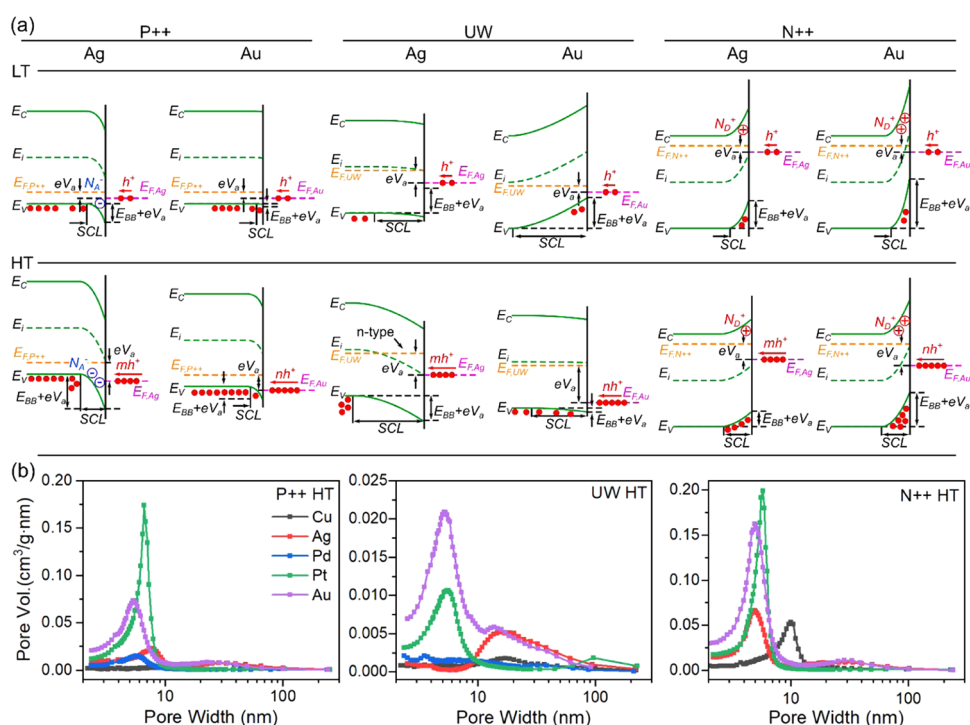


Figure 7. (a) Schematic energy band diagrams for Ag and Au LL-MACE of P++, UW, and N++ powders at low (LT, ice bath) and high (HT, water bath at 43 °C) temperatures. Number of injected holes at HT is larger than at LT and is different for Ag and Au. Due to hole accumulation in the metal, the quasi-Fermi level shifts downwards changing the band bending. The holes (h^+) are depicted as filled red dots, and the ionized donors ND^+ or acceptors NA^- in SCLs of N++ and P++ Si are depicted as open circles with a positive or negative sign, respectively. (b) BJH pore size distributions for all metals after LL-MACE of P++, UW, and N++ powders at HT.

490 MACE regardless of the type of metal because we always
491 perform LL-MACE with a value of ρ very close to 1.

492 As one can see, eq 2 does not include any information specific
493 to the metal catalyst, which our results demonstrate to play an
494 essential role in MACE. When VO_2^+ is used as an oxidant, the
495 chemical identity of the metal and its catalytic activity change the
496 mechanism of etching from the current-doubling pathway for Ag
497 and Au to a current-quadrupling pathway for Pt and a
498 combination of them for Pd.³² Unfortunately, the results for
499 H_2O_2 were less distinct, and in ref 32, it was concluded that the
500 effective valence can be affected by many factors including side
501 reactions, temperature, and metal coverage.

502 Table 2 summarizes the Fermi levels of Si powders used here
503 as well as metal work functions, magnitudes, widths, and
504 classification of band bending in the ideal scenario and
505 equilibrium conditions after metal deposition (no H_2O_2
506 injection). Details of the calculation of these parameters can
507 be found in Section S15, Supporting Information. The diameter
508 of the metal particles was set to 20 nm. A clear difference can be
509 observed for the p-type Si between Cu, Ag and Pd, Pt, Au. Due to
510 their low work function, Cu and Ag create a hole depletion
511 space-charge layer (SCL) in the p-type Si, while Pd, Pt, and Au
512 with sufficiently high work function such that $\Phi_M > \Phi_{Si}$ result in
513 hole accumulation and partly degenerate SCLs. Au on P++
514 powder is a particularly interesting case as there is almost no
515 band bending. This represents an Ohmic contact; it follows a
516 linear current–voltage curve and poses no barrier for charge
517 flow. For the n-type Si, all of the metals build up electron
518 depletion SCLs, and metals with high work function may result
519 in inversion layer formation. Note, however, that in real metal/Si
520 contacts the magnitude of band bending is significantly lower
521 than in the ideal case used for calculation here.³⁸ Therefore, it is

522 unlikely that in real samples inversion and degenerate parts of
523 SCLs are formed.

524 Overall, the magnitude of band bending depends on the
525 difference between the metal and Si work functions; the latter in
526 turn depends on the Si doping type and density. Additionally,
527 surface states can appear in the Si/metal interface, and the
528 density of these states may largely affect the Si Fermi level up to
529 the point where it gets pinned.⁵⁴ This, however, should not be
530 the case, as relatively defect-free hydrogen-terminated surfaces
531 form during MACE in HF-based solutions. Finally, H_2O_2
532 reduction injects holes and adsorbates can inject either electrons
533 or holes into metal particles; holes then accumulate in particles
534 due to an imbalance between hole generation, consumption,
535 and/or diffusion and make the particles charged. Charge
536 accumulation acts as an applied voltage bias and creates a
537 local electric field, which penetrates into Si as it cannot be
538 efficiently screened by the low concentration of charge carriers.
539 A potential drop at the Si/metal interface due to the bias can also
540 be viewed as a decrease of the quasi-Fermi level⁵⁵ in the metal,
541 thus favoring the holes to flow from metal to Si. The applied bias
542 can sufficiently affect band bending and even change the SCL
543 from, e.g., depletion to accumulation or the reverse.

544 Chiappini et al.³¹ showed the difference in porosity for Si
545 NWs after Ag and Au HL-MACE of the p-type Si at various
546 H_2O_2 concentrations. It is widely accepted that porosity is
547 introduced by remote etching, i.e., the nonlocal etching induced
548 by holes further away from their injection site at the metal/Si
549 interface. The tortuous pores in LL-MACE are due to remote
550 etching, and we demonstrate here that remote etching depends
551 heavily on band bending.

552 Herein, we discuss a model that considers the rate of hole
553 generation at the solution/metal interface and the rate of hole

554 escape from the metal/Si interface. The balance of these rates
 555 determines the balance between local and remote etching. We
 556 assume that the rate of escape does not influence the rate of
 557 generation. As we shall see, to a first approximation, this model
 558 explains the trends found in our data. A further refinement
 559 would include the potential for the coupling of these two rates.
 560 In LL-MACE, we used the same amount of H₂O₂ in all
 561 etchings. Thus, we assume that the role of H₂O₂ concentration
 562 in increasing carrier density is similar to that of temperature, in
 563 that either the increase of temperature or increase of H₂O₂
 564 concentration increases the availability of holes.^{33,57} Even
 565 though the total amount of injected H₂O₂ is independent of
 566 temperature, the rate of injection is higher at higher temper-
 567 atures because of faster diffusion and possible changes in the
 568 ratio of H₂O₂ used in hole injection versus side reactions. We
 569 further assume that each metal particle accumulates the same
 570 number of holes at each temperature independent of the Si
 571 doping type. For example, Ag accumulates holes at a certain rate
 572 at LT for all Si types and at a higher rate at HT, but again the rate
 573 is the same for all Si types. Also, Au accumulates holes at a
 574 different rate than Ag at LT and at HT, but still, the rate is the
 575 same for all Si types.

576 During H₂O₂ reduction, metal particles accumulate a positive
 577 charge, which acts as the applied potential and lowers the quasi-
 578 Fermi level of the metal. This in turn leads to a decrease of band
 579 bending in the presence of H₂O₂, $E_{\text{BB}}^{\text{H}_2\text{O}_2}$, by the value of eV_a from
 580 the ideal equilibrium values, E_{BB} , listed in Table 2

$$581 \quad E_{\text{BB}}^{\text{H}_2\text{O}_2} = E_{\text{BB}} + eV_a \quad (4)$$

582 where a potential V_a is gained due to accumulation of N_h holes
 583 and can be estimated as⁵⁰

$$584 \quad V_a = \frac{1}{4\pi\epsilon_0} \frac{eN_h}{r_M} \quad (5)$$

585 where ϵ_0 is the dielectric permittivity of vacuum, e is the
 586 elementary charge (positive), and r_M is the radius of the metal
 587 particle. With temperature increase, more holes accumulate in
 588 the metal lowering its quasi-Fermi level, increasing applied
 589 potential V_a , and decreasing band bending.

590 We first focus on explaining the differences between Ag and
 591 Au because these are the two most often used metals in HL-
 592 MACE, and in LL-MACE, they exhibit clearly distinctive pore
 593 size distributions. For P++ Si, Ag and Au at equilibrium create
 594 hole depletion and weak accumulation SCLs, respectively
 595 (Table 2). Accumulation of holes in the metal always results
 596 in the decrease of its quasi-Fermi level, thus either making
 597 depletion stronger, as for Ag, or creating a weak depletion SCL,
 598 as in the case of Au (Figure 7a). The striking difference between
 599 <10 nm pore volumes can be observed in Figures 7b and S9.1–
 600 S9.3, Supporting Information. In contrast, the volumes of etch
 601 track pores >10 nm produced by the metal particle movement
 602 are nearly identical. Thus, the availability of holes used for the
 603 above-critical-current etching near the particles is similar for Ag
 604 and Au, whereas the availability of holes that induce remote
 605 etching is minimal for Ag.

606 The Ag deposition-induced depletion SCL in P++ Si
 607 efficiently pushes the injected holes and holes present due to
 608 doping ($N_A = 4 \times 10^{18} \text{ cm}^{-3}$) away from the metal/Si interface.
 609 Part of the injected holes may additionally recombine with the
 610 fixed negatively charged acceptors N_A^- in the SCL. The layer is,
 611 however, rather thin (~10 nm, Table 2) due to high doping
 612 density. Thus, assuming the distance between 20 nm metal

particles is on the order of their size or larger,²⁰ there are regions
 of Si surface that are not affected by hole depletion. Combined
 with a high abundance of holes in the bulk and electric fields
 created by charged metal particles, holes can end up near the Si
 surface away from the SCL and, although not very efficient,
 nonetheless induce remote etching of tortuous pores. At HT,
 more holes get injected into the metal than at LT, decreasing the
 quasi-Fermi energy. This leads to the increase of potential eV_a ,
 making depletion even stronger while slightly increasing the
 width of SCL. On the other hand, correspondingly more holes
 are injected into Si resulting in a higher volume of tortuous pores
 at HT than at LT (graphs for Ag in Figure 4).

Band bending in P++ Si after Au deposition differs from that
 induced by Ag (Figure 6a). Since $\Phi_{\text{Au}} \sim \Phi_{\text{Si,P++}}$, a nearly Ohmic
 contact is formed with almost flat bands (weak accumulation
 SCL; Table 2). Thus, there should be no regions of Si where
 holes are unable to reach the Si surface and participate in remote
 etching. However, during H₂O₂ injection, a potential eV_a builds
 up that affects depletion layer formation, and at LT, the volume
 of pores <10 nm is small (Figures 4 and S9.1, Supporting
 Information). With the increase of temperature, more holes get
 injected, and due to much weaker and shorter depletion than in
 the case of Ag, a lot of tortuous pores are etched (Figures 4 and
 7).

Properties of SCLs in UW differ considerably from P++ Si. In
 addition to metal work functions, Si doping density affects two
 main parameters of the band bending. First, $E_{\text{F,UW}}$ is now close to
 the middle of the band gap, changing the value of $\Phi_{\text{Si,UW}} - \Phi_{\text{Si,P++}}$
 and, therefore, the magnitude of band bending. Second, low
 dopant density makes the SCL span over several micrometers
 (Table 2) covering the whole Si surface. Thus, there is no gap
 between metal particles where an SCL does not exist. Due to Φ_{Ag}
 $\sim \Phi_{\text{Si,UW}}$, a weak depletion layer is formed at equilibrium, which
 becomes stronger during the injection of H₂O₂ as the Ag quasi-
 Fermi level decreases. However, there are almost no free holes
 present in bulk UW Si compared to those in P++ Si, and all of the
 holes injected to Si either diffuse deep into the bulk or
 participate in local etching in the vicinity of Ag particles,
 producing only etch track pores (Figures 3 and S11.1,
 Supporting Information). High temperature makes depletion
 even stronger by an increase of eV_a . Thus, all holes, which did not
 participate in local etching, travel away from the Si surface, and
 no tortuous pores are etched (Figures 4 and 7).

The large work function of Au means that $\Phi_{\text{Au}} > \Phi_{\text{Si,UW}} > \Phi_{\text{Ag}}$
 and at equilibrium, Au creates a hole accumulation SCL in UW
 Si (Figure 7a). It is again spatially large as there are almost no
 holes from dopants to compensate the negative charge in Au.
 During H₂O₂ injection at LT, the magnitude of SCL somewhat
 decreases, which, however, is not enough to fully compensate
 the band bending. Thus, most of the holes accumulate at the Au/
 Si interface and are consumed for local etching of etch track
 pores (Figures 4 and S11.1, Supporting Information). The
 situation, however, changes significantly at HT when more holes
 are injected into Au, further lowering the magnitude of band
 bending. We assume that eV_a at HT becomes large enough to
 almost completely eliminate band bending, creating an Ohmic
 contact or a slight hole depletion layer. This would efficiently
 inject holes from Au into Si and spread them across the whole Si
 particle with virtually no barrier to approach the surface to
 participate in remote etching. We indeed clearly observed a
 significant increase of tortuous pore volume and specific surface
 area with the increase of temperature for UW Au LL-MACE
 (Figures 4 and S11.1–S11.3, Supporting Information).

676 Considering N++ powder, we note that there are extremely
677 few holes present at equilibrium in Si, and its $E_{F,N++}$ is quite close
678 to the conduction band, making $\Phi_{Si,N++} < \Phi_{Me}$ for all metals.
679 Thus, both Ag and Au create electron depletion layers consisting
680 of fixed ionized donors N_D^+ , which are positively charged
681 phosphorus atoms as their electrons diffused into the metal due
682 to differences in work functions (Figure 7a). When band
683 bending is strong enough, the intrinsic level E_i can cross $E_{F,N++}$.
684 Then, according to the definition of the p-type Si, N++ Si
685 changes from n-type to p-type in the area of SCL, where $E_i >$
686 $E_{F,N++}$. An inversion layer is formed for all of the metals except
687 Ag in the equilibrium conditions and ideal band bending. We,
688 however, point out again that the formation of an inversion layer
689 on real Si surfaces without the additional applied bias is highly
690 unlikely.³⁸ In most cases, only an electron depletion layer is built
691 up with a width of 8–10 nm instead of ~27 nm as listed in Table
692 2 for ideal band bending case (but see the discussion of Pd and
693 Pt after Ag and Au).

694 Similar to UW Si and if no inversion layer is formed, only the
695 holes available during LL-MACE of N++ Si with Ag and Au are
696 the holes injected first into the metal particles by H₂O₂
697 reduction, which subsequently diffused into Si. Herein, we
698 note the approximately twice higher volume of tortuous pores
699 etched by both Ag and Au in N++ Si compared to that of P++ Si
700 (Figures 4 and 6). We propose that in addition to SCL
701 differences, two other factors play significant roles here. The first
702 one is the charged donors in the N++ electron depletion SCL,
703 which may take part in LL-MACE and at least partially take a
704 role of holes to induce etching. Since donors are fixed in the Si
705 lattice, they are not susceptible to diffusion, and it can be shown
706 that all donors are ionized in the SCL.⁵⁴ The second and more
707 important factor is the many orders of magnitude larger hole
708 diffusion current in N++ compared to that in P++. To produce
709 the observed yields, the number of holes injected by H₂O₂
710 dissociation and consumed per Si particle during etching is on
711 the order of $4 \times 10^{10} \text{ s}^{-1}$. This value is slightly higher than $N_h =$
712 2.3×10^{10} per Si particle in P++ powder and 10^{17} times larger
713 than $N_h = 1.5 \cdot 10^{-7}$ per Si particle in N++ powder. Thus, in N++
714 Si due to the large difference between the density of injected
715 holes compared to the equilibrium density of holes, the SCL
716 cannot act as a reservoir to counteract the redistribution of these
717 holes from their site of injection. This leads to efficient hole
718 diffusion away from metal particles and etching of numerous
719 tortuous pores despite the recombination of injected holes with
720 bulk electrons.

721 Pd and Pt are the two metals with the largest work functions
722 among the set of metals studied. Both create upward band
723 bending independent of Si type, producing hole accumulation
724 layers in the p-type Si and electron depletion layers in the n-type
725 Si (Table 2). $\Phi_{Pt} > \Phi_{Pd}$ and consequently ideal magnitudes of
726 band bending are the highest for Pt. Thus, we cannot exclude the
727 formation of an inversion layer with mobile holes in N++ Si.
728 Indeed, we observed slow gas bubble generation for both Pt- and
729 Pd-deposited N++ Si even without H₂O₂ injection, which
730 indicated the presence of slow etching. No gas generation was
731 found for other Si grades and metals after deposition.

732 Pt was highly efficient in the etching of tortuous pores in all Si
733 grades with the highest values of $v_{\text{pore}}/v_{\text{etched}}$ (Figures 4, 5, and
734 S12.2, Supporting Information). We attribute this to several
735 factors. First, Pt particles tended to aggregate to a smaller
736 number of larger chunks (Figures 2 and 3); etching of etch track
737 pores by the aggregates was rather local, possibly due to the
738 prevalence of the current-quadrupling pathway for Pt MACE.³²

Second, the high magnitude of band bending resulted in hole
739 accumulation SCL for the p-type Si and buildup of an inversion
740 layer in the n-type Si. Finally, the SCLs are wide enough to span
741 between metal particles attracting holes to the Si surface and
742 inducing remote etching. The only metal that was able to
743 outperform Pt to create higher volumes of tortuous pores and
744 specific surface area was Au and only for UW at HT: 0.038 versus
745 $0.106 \text{ cm}^3 \cdot \text{g}^{-1}$ (Figures 4, 5, and 7b and Tables S6.4 and S7.4,
746 Supporting Information). We propose that the Pt-induced band
747 bending favors the injected hole accumulation near the Si
748 surface and makes more holes available for participation in
749 etching than for Au. With temperature increase, this leads to
750 increased local etching, which can be clearly observed by the
751 growth of the average pore size and decrease of $v_{\text{pore}}/v_{\text{etched}}$ ratio.
752 On the other hand, due to the large distance between aggregated
753 Pt particles, there is more Si without SCL where hole diffusion
754 current brings holes to produce tortuous pores. 755

The behavior of Pd is the most unique. Based on the
756 discussion above, it should produce porosity somewhere
757 between Au and Pt. However, this is not the case. Moreover,
758 25 μmol of Pd as used for other metals resulted in complete
759 dissolution of Si. Consequently, we used 2.5 μmol for all of the
760 etchings with Pd presented here, yet still, the outcome of LL-
761 MACE was very different. Electropolishing was observed for
762 UW powder at all temperatures, while for P++ wafer the volume
763 of tortuous pores decreased with increasing temperature (Figure
764 3 and Table S5.2, Supporting Information). For N++ powder,
765 etching was noticed after Pd deposition similar to Pt. Thus, Φ_{Pd}
766 may be high enough to create an inversion SCL in Si.
767 Additionally, Pd itself was found to be highly catalytically active
768 toward etching of Si even without oxidant injection, which was
769 attributed to the effects of dissolved O₂.⁵⁸ Consistent with the
770 concurrent etching by both valence 2 and valence 4 paths of
771 etching reported by Kolasinski et al.,³² Pd seems to catalyze
772 electropolishing instead of tortuous pore formation, especially at
773 HT. 774

Among all of the tested metals, Cu dissolves most readily
775 upon H₂O₂ injection because it has the lowest reduction
776 potential. For example, Cao et al.⁵⁹ measured nearly 90% Cu
777 mass reduction during the first 60 s of MACE. Therefore, no
778 HL-MACE was reported with Cu to produce ordered arrays of
779 etch track pores and Si NWs, although surface roughening was a
780 common outcome.^{60,61} Furthermore, the band bending induced
781 by Cu is similar to Ag; it is unfavorable for remote etching as a
782 depletion SCL is formed in the p-type Si (Table 2). For UW,
783 only etch track pores were observed analogous to Ag (Figure 4).
784 With temperature increase, the reduction of H₂O₂ becomes
785 faster and more Cu is dissolved than at LT. We associate the Cu
786 dissolution with a significant change of pore size distributions
787 with temperature for P++ and N++ powders and electro-
788 polishing for UW powder (Figures 4 and 7b) compared to other
789 metals. Therefore, only at LT, a reasonable volume of tortuous
790 pores was etched for P++ Si and etch track pores for UW Si. On
791 the other hand, the yield was 72 and 78% for P++ and UW,
792 respectively, clearly indicating only partial etching of Si particles
793 (Figures 2 and 5). When most of the Cu is dissolved, etching
794 may switch to a more regenerative electroless etching-like
795 mechanism.²⁷ In this case, Cu ions inject holes into Si directly
796 and then get regenerated by H₂O₂ to repeat the process. At HT,
797 the rate of injection increases, resulting in electropolishing, while
798 some etch track pores produced by large Cu particles are still
799 generated. 800

Intermediately doped P+, P, and N+ Si powders show nearly the same outcomes as UW Si for each metal (Figure 6). These results support the previous assumption that the injection of holes into Si is independent of Si grade and is determined mainly by the metal. Since the rate of holes that must be injected per Si particle is on the order of $4 \times 10^{10} \text{ s}^{-1}$, which is much larger than the number of dopant atoms in the particle, there is a large gradient in hole concentration between the metal nanoparticle and bulk Si. The large gradient then drives the diffusion of holes from the metal into the Si bulk, and some of the holes re-emerge near the Si surface to induce remote etching. The appearance of holes far from metal nanoparticles near the Si surface is in turn governed by the type of SCL, magnitude of the electric field in it, and SCL width. For P+, P, UW, and N+ powders, SCL width becomes large enough to leave no gaps between metal nanoparticles (Table 2). Thus, depending on the type of SCL, holes get effectively pushed into the bulk by the electric field (as for Cu and Ag) or stay close to metal nanoparticles (as for Pd, Pt, and Au). Only when there are enough holes accumulated in Au at HT and the magnitude of band bending on the Si/Au interface along with the electric field is decreased, holes are able to diffuse further from metal nanoparticles and tortuous pores start to appear. Pt is the exception here; it produces tortuous pores for all Si grades and at all temperatures (Figures 4 and 6 and Section S6, Supporting Information). In our view, this is due to upward band bending in all Si grades and large size of Pt nanoparticle aggregates. The latter results in the parts of Si surface not affected by SCL.

The rate of hole generation in metal nanoparticles, their charging, and further diffusion of holes into Si are affected by H_2O_2 concentration near the nanoparticles. During etching, the H_2O_2 needs to diffuse from the injection site in the solution, thus making the H_2O_2 concentration in the pores unknown. The size of metal nanoparticles and correspondingly the size of etch track pores may therefore play an important role in the transport of H_2O_2 and other species involved in etching. For example, a few large metal nanoparticles (as in the case of Pt) generate wider etch track pores that facilitate a faster influx of etchant and efflux of etch products. A steady-state concentration gradient may be reached around metal particles in the tortuous pores due to the balance between the reaction and diffusion rates. Concentration gradient profiles can be further affected by, e.g., temperature, metal catalyst, pore size, and depth and contribute to the pore morphology of the product.

To summarize, LL-MACE resulted in distinctive specific surface areas, yields, and pore volumes depending on the Si grade, metal catalyst, and temperature. Three major factors have been identified that contribute to the distinctive features of LL-MACE:

(1) Band bending and space-charge layer (SCL) formation clearly play a significant role in defining the observed outcomes. A distinct difference exists between the highly doped nearly metallic Si and moderately doped Si. The SCL width in relation to the distance between metal nanoparticles is crucial. The SCL is narrow for N++ and P++ Si, leaving gaps on the Si surface between metal nanoparticles without the electric field. For HL-MACE, it is believed that remote etching is only important in P++ Si. In LL-MACE, we find that the orders of magnitudes larger gradient of hole concentration in N++ facilitate high hole diffusion current and efficient remote etching.

(2) Chemical, not just electronic, differences between metals lead to distinctive behaviors. Dissolution and redeposition of metal nanoparticles affect the nanoparticle structure during etching, which in turn affects the resulting pore size distributions. We observed peculiar comet-like structures of Cu, Pd, and Pt particles (Figure 2), which unambiguously demonstrates the dynamic nature of metal nanoparticles. The comet-like structure is not required for remote etching because Au never shows a comet-like structure and Pt does not always show it even though they are efficient catalysts of remote etching. The reactivity of Pd is unique, and it must be used at a lower coverage than the other metals to enable porosification.

(3) Mass transport and concentration of H_2O_2 affect the rates of both etching and metal nanoparticle dissolution and are important for morphological evolution. Cu is the most easily dissolving metal, and at high temperature, it catalyzes electropolishing rather than porosification. Nonetheless, a low concentration of H_2O_2 achieved with controlled injection and low temperature enables highly efficient and controllable LL-MACE also with Cu (Figures 3 and 4).

CONCLUSIONS

Our comprehensive study has illuminated the mechanisms of MACE and enhanced our ability to exploit it for technical applications. We built upon the recognition of the role of band bending in Si³⁹ in the vicinity of deposited metal nanoparticles^{38,62} to gain control over the structures formed by etching. We show that band bending alone is unable to fully describe the observed LL-MACE outcomes. Instead, the chemical identity of metals, their catalytic activity toward the reduction of H_2O_2 , the ability to induce different etching pathways, and the tendency to dissolve all influence the results of etching. We demonstrated the generality of LL-MACE and that it can be applied to any kind of Si. Moreover, the judicious choice of the etching parameters (including H_2O_2 concentration, metal catalyst, temperature, and the type and density of Si doping) facilitates considerable control of the mean pore size, surface areas, and pore volumes of etched Si powders. The large variety of accessible surface areas, pore sizes, and pore volumes combined with high scalability and economical use of reagents will make LL-MACE highly appealing for use in both research and industry.

ASSOCIATED CONTENT

Supporting Information

The Supporting Information is available free of charge at <https://pubs.acs.org/doi/10.1021/acsami.0c13980>.

Experimental details, description of band bending calculation, and detailed etching data for all Si types including metallurgical-grade Si (PDF)

AUTHOR INFORMATION

Corresponding Author

Kurt W. Kolasinski – Department of Chemistry, West Chester University, West Chester, Pennsylvania 19383-2115, United States; orcid.org/0000-0002-9469-2700; Email: KKolasinski@wcupa.edu

918 **Authors**

- 919 **Konstantin Tamarov** – Department of Applied Physics,
920 University of Eastern Finland, 70210 Kuopio, Finland;
921 orcid.org/0000-0003-0087-4878
- 922 **Riku Kiviluoto** – Department of Applied Physics, University of
923 Eastern Finland, 70210 Kuopio, Finland
- 924 **Joseph D. Swanson** – Department of Chemistry, West Chester
925 University, West Chester, Pennsylvania 19383-2115, United
926 States
- 927 **Bret A. Unger** – Department of Chemistry, West Chester
928 University, West Chester, Pennsylvania 19383-2115, United
929 States
- 930 **Alexis T. Ernst** – Department of Materials Science and
931 Engineering, Institute of Materials Science, University of
932 Connecticut, Storrs, Connecticut 06269-3136, United States
- 933 **Mark Aindow** – Department of Materials Science and
934 Engineering, Institute of Materials Science, University of
935 Connecticut, Storrs, Connecticut 06269-3136, United States;
936 orcid.org/0000-0001-6617-1409
- 937 **Joakim Riikonen** – Department of Applied Physics, University of
938 Eastern Finland, 70210 Kuopio, Finland; orcid.org/0000-0002-5304-9479
- 939 **Vesa-Pekka Lehto** – Department of Applied Physics, University of
940 Eastern Finland, 70210 Kuopio, Finland; orcid.org/0000-0001-8153-1070

943 Complete contact information is available at:
944 <https://pubs.acs.org/10.1021/acsami.0c13980>

945 **Author Contributions**

946 The manuscript was written through the contributions of all
947 authors. All authors have given approval to the final version of
948 the manuscript.

949 **Funding**

950 Funding provided by grants #314552 and #314412 from the
951 Academy of Finland and the National Science Foundation
952 award #1825331.

953 **Notes**

954 The authors declare no competing financial interest.

955 ■ **ACKNOWLEDGMENTS**

956 The microscopy studies were performed using the facilities in
957 the UConn/Thermo Fisher Scientific Center for Advanced
958 Microscopy and Materials Analysis (CAMMA) and SIB Labs,
959 Laboratory of Microscopy, at the University of Eastern Finland.
960 Silicon was provided by Elkem Silicon Materials and Okmetic.

961 ■ **REFERENCES**

- 962 (1) Peng, K. Q.; Lee, S. T. Silicon Nanowires for Photovoltaic Solar
963 Energy Conversion. *Adv. Mater.* **2011**, *23*, 198–215.
- 964 (2) Otto, M.; Algasinger, M.; Branz, H.; Gesemann, B.; Gimpel, T.;
965 Fücksel, K.; Käsebier, T.; Kontermann, S.; Koynov, S.; Li, X.;
966 Naumann, V.; Oh, J.; Sprafke, A. N.; Ziegler, J.; Zilk, M.; Wehrspohn,
967 R. B. Black Silicon Photovoltaics. *Adv. Opt. Mater.* **2015**, *3*, 147–164.
- 968 (3) Toor, F.; Miller, J. B.; Davidson, L. M.; Duan, W.; Jura, M. P.; Yim,
969 J.; Forziati, J.; Black, M. R. Metal Assisted Catalyzed Etched (MACE)
970 Black Si: Optics and Device Physics. *Nanoscale* **2016**, *8*, 15448–15466.
- 971 (4) Sainato, M.; Strambini, L. M.; Rella, S.; Mazzotta, E.; Barillaro, G.
972 Sub-Parts per Million NO₂ Chemi-Transistor Sensors Based on
973 Composite Porous Silicon/Gold Nanostructures Prepared by Metal-
974 Assisted Etching. *ACS Appl. Mater. Interfaces* **2015**, *7*, 7136–7145.
- 975 (5) Balderas-Valadez, R. F.; Agarwal, V.; Pacholski, C. Fabrication of
976 Porous Silicon-Based Optical Sensors Using Metal-Assisted Chemical
977 Etching. *RSC Adv.* **2016**, *6*, 21430–21434.

- (6) Georgobiani, V. A.; Gonchar, K. A.; Zvereva, E. A.; Osminkina, L. 978
A. Porous Silicon Nanowire Arrays for Reversible Optical Gas Sensing. 979
Phys. Status Solidi A **2018**, *215*, No. 1700565. 980
- (7) Zamfir, M. R.; Nguyen, H. T.; Moyen, E.; Lee, Y. H.; Pribat, D. 981
Silicon Nanowires for Li-Based Battery Anodes: A Review. *J. Mater.* 982
Chem. A **2013**, *1*, 9566–9586. 983
- (8) Li, X.; Yan, C.; Wang, J.; Graff, A.; Schweizer, S. L.; Sprafke, A.; 984
Schmidt, O. G.; Wehrspohn, R. B. Stable Silicon Anodes for Lithium- 985
Ion Batteries Using Mesoporous Metallurgical Silicon. *Adv. Energy* 986
Mater. **2015**, *5*, No. 1401556. 987
- (9) McSweeney, W.; Geaney, H.; O'Dwyer, C. Metal-Assisted 988
Chemical Etching of Silicon and the Behavior of Nanoscale Silicon 989
Materials as Li-Ion Battery Anodes. *Nano Res.* **2015**, *8*, 1395–1442. 990
- (10) Han, H.; Kim, J.; Shin, H. S.; Song, J. Y.; Lee, W. Air-Bridged 991
Ohmic Contact on Vertically Aligned Si Nanowire Arrays: Application 992
to Molecule Sensors. *Adv. Mater.* **2012**, *24*, 2284–2288. 993
- (11) Chiappini, C.; De Rosa, E.; Martinez, J. O.; Liu, X.; Steele, J.; 994
Stevens, M. M.; Tasciotti, E. Biodegradable Silicon Nanoneedles 995
Delivering Nucleic Acids Intracellularly Induce Localized in Vivo 996
Neovascularization. *Nat. Mater.* **2015**, *14*, 532–539. 997
- (12) Harding, F. J.; Surdo, S.; Delalat, B.; Cozzi, C.; Elnathan, R.; 998
Gronthos, S.; Voelcker, N. H.; Barillaro, G. Ordered Silicon Pillar 999
Arrays Prepared by Electrochemical Micromachining: Substrates for 1000
High-Efficiency Cell Transfection. *ACS Appl. Mater. Interfaces* **2016**, *8*, 1001
29197–29202. 1002
- (13) Osminkina, L. A.; Sivakov, V. A.; Mysov, G. A.; Georgobiani, V. 1003
A.; Natashina, U.A.; Talkenberg, F.; Solov'yev, V. V.; Kudryavtsev, A. A.; 1004
Timoshenko, V. Y. Nanoparticles Prepared from Porous Silicon 1005
Nanowires for Bio-Imaging and Sonodynamic Therapy. *Nanoscale* 1006
Res. Lett. **2014**, *9*, 463. 1007
- (14) Peng, F.; Su, Y.; Wei, X.; Lu, Y.; Zhou, Y.; Zhong, Y.; Lee, S.-T.; 1008
He, Y. Silicon-Nanowire-Based Nanocarriers with Ultrahigh Drug- 1009
Loading Capacity for In Vitro and In Vivo Cancer Therapy. *Angew.* 1010
Chem., Int. Ed. **2013**, *52*, 1457–1461. 1011
- (15) Peng, F.; Su, Y.; Ji, X.; Zhong, Y.; Wei, X.; He, Y. Doxorubicin- 1012
Loaded Silicon Nanowires for the Treatment of Drug-Resistant Cancer 1013
Cells. *Biomaterials* **2014**, *35*, 5188–5195. 1014
- (16) Huang, Z.; Geyer, N.; Werner, P.; de Boor, J.; Gösele, U. Metal- 1015
Assisted Chemical Etching of Silicon: A Review. *Adv. Mater.* **2011**, *23*, 1016
285–308. 1017
- (17) Chen, C.-Y.; Wei, T.-C.; Hsiao, P.-H.; Hung, C.-H. Vanadium 1018
Oxide as Transparent Carrier-Selective Layer in Silicon Hybrid Solar 1019
Cells Promoting Photovoltaic Performances. *ACS Appl. Energy Mater.* 1020
2019, *2*, 4873–4881. 1021
- (18) Putra, I. R.; Li, J.-Y.; Chen, C.-Y. 18.78% Hierarchical Black 1022
Silicon Solar Cells Achieved with the Balance of Light-Trapping and 1023
Interfacial Contact. *Appl. Surf. Sci.* **2019**, *478*, 725–732. 1024
- (19) Kolasinski, K. W.; Unger, B. A.; Ernst, A. T.; Aindow, M. 1025
Crystallographically Determined Etching and Its Relevance to the 1026
Metal-Assisted Catalytic Etching (MACE) of Silicon Powders. *Front.* 1027
Chem. **2019**, *6*, No. 651. 1028
- (20) Tamarov, K. P.; Swanson, J. D.; Unger, B. A.; Kolasinski, K. W.; 1029
Ernst, A. T.; Aindow, M.; Lehto, V.-P.; Riikonen, J. Controlling the 1030
Nature of Etched Si Nanostructures: High versus Low Load Metal- 1031
Assisted Catalytic Etching (MACE) of Si Powders. *ACS Appl. Mater.* 1032
Interfaces **2020**, *12*, 4787–4796. 1033
- (21) Li, X.; Xiao, Y.; Yan, C.; Zhou, K.; Miclea, P. T.; Meyer, S.; 1034
Schweizer, S. L.; Sprafke, A.; Lee, J. H.; Wehrspohn, R. B. Self- 1035
Purification Model for Metal-Assisted Chemical Etching of Metal- 1036
lurgical Silicon. *Electrochim. Acta* **2014**, *138*, 476–480. 1037
- (22) Xi, F.; Li, S.; Ma, W.; Ding, Z.; Lei, Y.; Chen, Z.; Wei, K.; Xie, K.; 1038
Wu, J. Removal of Impurities from Metallurgical Grade Silicon with 1039
Metal Assisted Chemical Leaching. *Hydrometallurgy* **2018**, *178*, 250– 1040
255. 1041
- (23) Liu, Y.; Chen, B.; Cao, F.; Chan, H. L. W.; Zhao, X.; Yuan, J. One- 1042
Pot Synthesis of Three-Dimensional Silver-Embedded Porous Silicon 1043
Microparticles for Lithium-Ion Batteries. *J. Mater. Chem.* **2011**, *21*, 1044
17083–17086. 1045

- (24) Bang, B. M.; Kim, H.; Song, H.-K.; Cho, J.; Park, S. Scalable Approach to Multi-Dimensional Bulk Si Anodes via Metal-Assisted Chemical Etching. *Energy Environ. Sci.* **2011**, *4*, 5013–5019.
- (25) Li, X.; Xiao, Y.; Bang, J. H.; Lausch, D.; Meyer, S.; Miclea, P.; Jung, J.; Schweizer, S. L.; Lee, J.; Wehrspohn, R. B. Upgraded Silicon Nanowires by Metal-Assisted Etching of Metallurgical Silicon: A New Route to Nanostructured Solar-Grade Silicon. *Adv. Mater.* **2013**, *25*, 3187–3191.
- (26) Kozlov, N. K.; Natashina, U. A.; Tamarov, K. P.; Gongalsky, M. B.; Solovyev, V. V.; Kudryavtsev, A. A.; Sivakov, V.; Osminkina, L. A. Recycling of Silicon: From Industrial Waste to Biocompatible Nanoparticles for Nanomedicine. *Mater. Res. Express* **2017**, *4*, No. 095026.
- (27) Kolasinski, K. W.; Gimbar, N. J.; Yu, H.; Aindow, M.; Mäkilä, E.; Salonen, J. Regenerative Electroless Etching of Silicon. *Angew. Chem., Int. Ed.* **2017**, *56*, 624–627.
- (28) Alhmod, H.; Brodoceanu, D.; Elnathan, R.; Kraus, T.; Voelcker, H. A. MACEing Silicon: Towards Single-Step Etching of Defined Porous Nanostructures for Biomedicine. *Prog. Mater. Sci.* **2019**, *106*, No. 100636.
- (29) Geyer, N.; Wollschläger, N.; Fuhrmann, B.; Tonkikh, A.; Berger, A.; Werner, P.; Jungmann, M.; Krause-Rehberg, R.; Leipner, H. S. Influence of the Doping Level on the Porosity of Silicon Nanowires Prepared by Metal-Assisted Chemical Etching. *Nanotechnology* **2015**, *26*, No. 245301.
- (30) Georgobiani, V. A.; Gonchar, K. A.; Osminkina, L. A.; Timoshenko, V. Y. Structural and Photoluminescent Properties of Nanowires Formed by the Metal-Assisted Chemical Etching of Monocrystalline Silicon with Different Doping Level. *Semiconductors* **2015**, *49*, 1025–1029.
- (31) Chiappini, C.; Liu, X.; Fakhoury, J. R.; Ferrari, M. Biodegradable Porous Silicon Barcode Nanowires with Defined Geometry. *Adv. Funct. Mater.* **2010**, *20*, 2231–2239.
- (32) Kolasinski, K. W.; Barclay, W. B.; Sun, Y.; Aindow, M. The Stoichiometry of Metal Assisted Etching (MAE) of Si in $V_2O_5 + HF$ and $HOOH + HF$ Solutions. *Electrochim. Acta* **2015**, *158*, 219–228.
- (33) Kolasinski, K. W. Electron Transfer during Metal-Assisted and Stain Etching of Silicon. *Semicond. Sci. Technol.* **2016**, *31*, No. 014002.
- (34) Yae, S.; Tashiro, M.; Hirano, T.; Abe, M.; Fukumuro, N.; Matsuda, H. High Catalytic Activity of Palladium for Metal-Enhanced Hydrofluoric Acid Etching of Silicon. *ECS Trans.* **2009**, *16*, 285–289.
- (35) Lee, J. P.; Choi, S.; Park, S. Extremely Superhydrophobic Surfaces with Micro- and Nanostructures Fabricated by Copper Catalytic Etching. *Langmuir* **2011**, *27*, 809–814.
- (36) Guan, B.; Sun, Y.; Li, X.; Wang, J.; Chen, S.; Schweizer, S.; Wang, Y.; Wehrspohn, R. B. Conversion of Bulk Metallurgical Silicon into Photocatalytic Nanoparticles by Copper-Assisted Chemical Etching. *ACS Sustainable Chem. Eng.* **2016**, *4*, 6590–6599.
- (37) Huang, Z. P.; Geyer, N.; Liu, L. F.; Li, M. Y.; Zhong, P. Metal-Assisted Electrochemical Etching of Silicon. *Nanotechnology* **2010**, *21*, 1096 No. 465301.
- (38) Kolasinski, K. W. The Mechanism of Galvanic/Metal-Assisted Etching of Silicon. *Nanoscale Res. Lett.* **2014**, *9*, No. 432.
- (39) Torralba, E.; Le Gall, S.; Lachaume, R.; Magnin, V.; Harari, J.; Halbwax, M.; Vilcot, J.-P.; Cachet-Vivier, C.; Bastide, S. Tunable Surface Structuration of Silicon by Metal Assisted Chemical Etching with Pt Nanoparticles under Electrochemical Bias. *ACS Appl. Mater. Interfaces* **2016**, *8*, 31375–31384.
- (40) Kolasinski, K. W. The Mechanism of Si Etching in Fluoride Solutions. *Phys. Chem. Chem. Phys.* **2003**, *5*, 1270–1278.
- (41) Hochbaum, A. I.; Gargas, D.; Hwang, Y. J.; Yang, P. Single Crystalline Mesoporous Silicon Nanowires. *Nano Lett.* **2009**, *9*, 3550–3554.
- (42) Patil, J. J.; Smith, B. D.; Grossman, J. C. Ultra-High Aspect Ratio Functional Nanoporous Silicon via Nucleated Catalysts. *RSC Adv.* **2017**, *7*, 11537–11542.
- (43) Klaassen, D. B. M. A Unified Mobility Model for Device Simulation—I. Model Equations and Concentration Dependence. *Solid. State. Electron.* **1992**, *35*, 961–967.
- (44) Kolasinski, K. W.; Barclay, W. B. The Stoichiometry of Electroless Silicon Etching in Solutions of V_2O_5 and HF. *Angew. Chem., Int. Ed.* **2013**, *52*, 6731–6734.
- (45) Kolasinski, K. W. Silicon Nanostructures from Electroless Electrochemical Etching. *Curr. Opin. Solid State Mater. Sci.* **2005**, *9*, 73–83.
- (46) Gondek, C.; Lippold, M.; Röver, I.; Bohmhammel, K.; Kroke, E. Etching Silicon with HF-H₂O₂-Based Mixtures: Reactivity Studies and Surface Investigations. *J. Phys. Chem. C* **2014**, *118*, 2044–2051.
- (47) Sadakane, D.; Yamakawa, K.; Fukumuro, N.; Yae, S. Catalytic Activity of Ru for Metal-Assisted Etching of Si. *ECS Trans.* **2015**, *69*, 179–184.
- (48) Yae, S.; Morii, Y.; Fukumuro, N.; Matsuda, H. Catalytic Activity of Noble Metals for Metal-Assisted Chemical Etching of Silicon. *Nanoscale Res. Lett.* **2012**, *7*, No. 352.
- (49) Stafiniak, A.; Prazmowska, J.; Macherzyński, W.; Paszkiewicz, R. Nanostructuring of Si Substrates by a Metal-Assisted Chemical Etching and Dewetting Process. *RSC Adv.* **2018**, *8*, 31224–31230.
- (50) Wang, J.; Hu, Y.; Zhao, H.; Fu, H.; Wang, Y.; Huo, C.; Peng, K. Q. Oxidant Concentration Modulated Metal/Silicon Interface Electrical Field Mediates Metal-Assisted Chemical Etching of Silicon. *Adv. Mater. Interfaces* **2018**, *5*, No. 1801132.
- (51) Chartier, C.; Bastide, S.; Lévy-Clément, C. Metal-Assisted Chemical Etching of Silicon in HF-H₂O₂. *Electrochim. Acta* **2008**, *53*, 5509–5516.
- (52) Xia, X. H.; Ashruf, C. M. A.; French, P. J.; Kelly, J. J. Galvanic Cell Formation in Silicon/Metal Contacts: The Effect on Silicon Surface Morphology. *Chem. Mater.* **2000**, *12*, 1671–1678.
- (53) Kooij, E. S.; Vanmaekelbergh, D. Catalysis and Pore Initiation in the Anodic Dissolution of Silicon in HF. *J. Electrochem. Soc.* **1997**, *144*, 1296–1301.
- (54) Lüth, H. Space-Charge Layers at Semiconductor Interfaces. In *Solid Surfaces, Interfaces and Thin Films*; Springer, 2015; pp 337–391.
- (55) Streetman, B. G.; Banerjee, S. K. *Solid State Electronic Devices*, 6th ed.; Pearson Education, Inc., 2006.
- (56) *CRC Handbook of Chemistry and Physics*, 95th ed.; Haynes, W. M., Ed.; CRC Press: Boca Raton, FL, 2014.
- (57) Kolasinski, K. W.; Gogola, J. W.; Barclay, W. B. Test of Marcus Theory Predictions for Electroless Etching of Silicon. *J. Phys. Chem. C* **2012**, *116*, 21472–21481.
- (58) Yae, S.; Tashiro, M.; Abe, M.; Fukumuro, N.; Matsuda, H. High Catalytic Activity of Palladium for Metal-Enhanced HF Etching of Silicon. *J. Electrochem. Soc.* **2010**, *157*, D90.
- (59) Cao, M.; Li, S. Y.; Deng, J. X.; Yang, X. W.; Li, Y. P.; Ma, W. H.; Zhou, Y. Preparation of Large-Area Porous Silicon through Cu-Assisted Chemical Etching. *Mater. Sci. Forum* **2016**, *847*, 78–83.
- (60) Toor, F.; Oh, J.; Branz, H. M. Efficient Nanostructured ‘Black’ Silicon Solar Cell by Copper-Catalyzed Metal-Assisted Etching. *Prog. Photovoltaics* **2015**, *23*, 1375–1380.
- (61) Zheng, H.; Han, M.; Zheng, P.; Zheng, L.; Qin, H.; Deng, L. Porous Silicon Templates Prepared by Cu-Assisted Chemical Etching. *Mater. Lett.* **2014**, *118*, 146–149.
- (62) Lai, R. A.; Hymel, T. M.; Narasimhan, V. K.; Cui, Y. Schottky Barrier Catalysis Mechanism in Metal-Assisted Chemical Etching of Silicon. *ACS Appl. Mater. Interfaces* **2016**, *8*, 8875–8879.